Simulations of Polarimetric Radar Signatures of a Supercell Storm Using a Two-Moment Bulk Microphysics Scheme

YOUNGSUN JUNG AND MING XUE

School of Meteorology, and Center for Analysis and Prediction of Storms, University of Oklahoma, Norman, Oklahoma

GUIFU ZHANG

School of Meteorology, University of Oklahoma, Norman, Oklahoma

(Manuscript received 6 January 2009, in final form 6 July 2009)

ABSTRACT

A new general polarimetric radar simulator for nonhydrostatic numerical weather prediction (NWP) models has been developed based on rigorous scattering calculations using the T-matrix method for reflectivity, differential reflectivity, specific differential phase, and copolar cross-correlation coefficient. A continuous melting process accounts for the entire spectrum of varying density and dielectric constants. This simulator is able to simulate polarimetric radar measurements at weather radar frequency bands and can take as input the prognostic variables of high-resolution NWP model simulations using one-, two-, and three-moment microphysics schemes. The simulator was applied at 10.7-cm wavelength to a model-simulated supercell storm using a double-moment (two moment) bulk microphysics scheme to examine its ability to simulate polarimetric signatures reported in observational studies. The simulated fields exhibited realistic polarimetric signatures that include Z_{DR} and K_{DP} columns, Z_{DR} arc, midlevel Z_{DR} and ρ_{hv} rings, hail signature, and K_{DP} foot in terms of their general location, shape, and strength. The authors compared the simulation with one employing a single-moment (SM) microphysics scheme and found that certain signatures, such as Z_{DR} arc, midlevel Z_{DR}, and ρ_{hv} rings, cannot be reproduced with the latter. It is believed to be primarily caused by the limitation of the SM scheme in simulating the shift of the particle size distribution toward larger/smaller diameters, independent of mixing ratio. These results suggest that two- or higher-moment microphysics schemes should be used to adequately describe certain important microphysical processes. They also demonstrate the utility of a well-designed radar simulator for validating numerical models. In addition, the simulator can also serve as a training tool for forecasters to recognize polarimetric signatures that can be reproduced by advanced NWP models.

1. Introduction

Supercell thunderstorms have received significant attention from the meteorology community because they often cause serious damage from the associated tornadoes, large hail, strong winds, and/or heavy precipitation. Many observational studies have focused mainly on understanding the time evolution of storm structure, microphysical characteristics, and dynamics using radar reflectivity and radial velocity data (e.g., Browning and Donaldson 1963; Browning 1964; Lemon and Doswell 1979; Marwitz 1972; Musil et al. 1986; Ray et al. 1981; Brandes 1978, 1984, 1993). Numerical studies have tried to simulate such supercell storms and aid in the understanding of storm evolution and dynamics (e.g., Klemp and Wilhelmson 1978; Klemp et al. 1981; Weisman and Klemp 1982; Rotunno 1981; Klemp and Weisman 1983). Recently, research has demonstrated that the storm microphysical processes and properties can be better understood with polarimetric radar data (e.g., Bringi et al. 1986; Hubbert et al. 1998; Romine et al. 2008; Kumjian and Ryzhkov 2008, 2009, hereinafter KR08 and KR09, respectively).

Although conventional and polarimetric radar observations offer important insights into storms, observations are often insufficient to provide details on the storms because of various limitations. Such limitations

Corresponding author address: Youngsun Jung, Center for Analysis and Prediction of Storms, National Weather Center, Suite 2500, 120 David L. Boren Blvd., Norman, OK 73072.
E-mail: youngsun.jung@ou.edu

DOI: 10.1175/2009JAMC2178.1

include the lack of complete spatial coverage because of beam blockage, radar cone of silence, or lack of signal returns in weak echo regions, sampling noise and signal attenuation, or insufficient spatial and temporal resolutions. In addition to these external factors, reflectivity and polarimetric measurements provide only high-moment bulk properties of all hydrometeors in the radar resolution volume, and Doppler radial velocity offers only the wind component projected in the direction of the radar beams.

On the other hand, numerical models allow meteorologists to study details that are not directly observed by current observational platforms with high temporal and spatial resolutions. They can help substantiate findings from observational studies. Numerical models also can be used to help develop new theories. Most of all, the numerical model is of primary importance in modern weather forecasting. However, the numerical solutions must be validated with appropriate observations; a complementary relationship exists between observations and numerical models.

For direct comparisons between model output and radar observations, the model variables are often converted into the form of observations using a radar simulator (Jung et al. 2008a, hereinafter JZX08; Pfeifer et al. 2008), which also acts as the forward observation operator in data assimilation systems. The radar simulator should be accurate, consistent with model microphysics, and make use of all relevant information available in the model.

Most existing polarimetric radar simulators deal only with rain or dry ice exclusively (e.g., Brandes et al. 2004; Ryzhkov et al. 1998; Vivekanandan et al. 1994; Zhang et al. 2001; Capsoni et al. 2001); the literature covers only a handful of complete polarimetric radar simulators that utilize a full set of parameters available in the numerical model. Huang et al. (2005), in a short conference paper, reported on a simulator based on T-matrix scattering calculations (Waterman 1969; Vivekanandan et al. 1991). It used output from the Regional Atmospheric Modeling System (RAMS) employing a two-moment microphysics scheme (Walko et al. 1995; Meyers et al. 1997). In that paper, the authors employed a simple melting treatment for ice species with fixed fractions of water and ice (and air for graupel) based on the height or air temperature.

Recently, JZX08 developed a polarimetric radar simulator utilizing the fitting of the scattering amplitudes of rain calculated using T-matrix codes in a power-law form of the particle size, while Rayleigh scattering approximation is used for ice for a single-moment microphysics scheme. In the work, the authors introduced a new melting ice model with a continuously varying density of ice particles and the fractional water in the ice. In this melting ice model, wet ice particles, such as rain–snow or rain–hail mixtures, are constructed when rainwater coexists with snow or hail. In the model, the fractional water in the ice is determined by the relative amount between rainwater and snow or hail. For the data assimilation purpose reported in that paper, the researchers had to use curves fitted to precalculated data or Rayleigh scattering assumption in the simulator for efficiency; therefore, it is not a general purpose simulator.

Pfeifer et al. (2008) also proposed a polarimetric simulator called Synthetic Polarimetric Radar (SynPolRad) based on the T-matrix method. SynPolRad is coupled with a single-moment microphysics scheme with various assumptions about the hydrometeor drop size distributions (DSDs). The authors determined a fixed value for water fraction in wet ice hydrometeors by fitting the values of simulated polarimetric variables to their expected values within a certain range of observations. However, the dielectric model used by them is physically questionable because the dielectric constant was calculated ''as water inside an ice matrix inside air matrix,'' which cannot correctly represent the significant contribution from the meltwater shell. Additionally, the specific differential phase, which is a very useful polarimetric measurement, is not included in SynPolRad.

Although these simulators have their own strengths and weaknesses, they show that polarimetric radar simulators can be useful for evaluating model microphysics. Furthermore, a computationally optimized simulator can serve as the forward observation operator in data assimilation systems.

In this study, we develop a radar simulator that is more general than that described in JZX08; it employs the full T-matrix scattering method for both rain and ice hydrometeors and allows for the specification of any radar wavelength for scattering calculations. In this study, the wavelength is set to 10.7 cm, that of the U.S. operational Weather Surveillance Radar-1988 Doppler (WSR-88D) radars. Model prognostic variables associated with single-, double-, or three-moment (SM, DM, and TM, respectively) bulk microphysics schemes (simply ''scheme'' hereinafter) can be used as inputs. The polarimetric variables simulated include reflectivity at the horizontal and vertical polarizations (Z_H and Z_V), differential reflectivity $Z_{\rm DR}$, specific differential phase $K_{\rm DP}$, and the copolar cross-correlation coefficient at zero-lag $\rho_{hv}(0)$.

A recent study of Milbrandt and Yau (2006), Dawson et al. (2007, 2010), and Dawson (2009) found that supercell thunderstorms with a more realistic reflectivity structure and cold pool strength can be obtained with a multimoment (MM) microphysics scheme, with most improvement achieved when moving from SM to DM

scheme. Their results show that the DM and TM simulations are qualitatively similar in terms of cold pool structure, reflectivity pattern in the forward flank regions, the amount of total cooling in the low-level downdraft, the characteristics of drop size distribution parameters, and the origin of the air in the surface cold pool. On the other hand, the SM runs show large variability within these runs, depending on the choice of the intercept parameter values. Briefly, the MM schemes produce weaker and moister cold pools and more extended forward flank regions. Their trajectory analyses show that the air near the surface cold pool originates from above the boundary layer (2–3 km AGL) in the SM runs while it comes from about 1 km AGL in the MM runs. The mean-mass diameter of raindrops in the low-level downdraft is significantly larger in the MM runs than in the SM runs. These results show that the storm microphysics evolve in very different ways in the SM and MM schemes. The polarimetric measurement may provide an additional means to evaluate the performance of different microphysics schemes.

In this study, we apply our newly developed simulator to a supercell storm simulated using DM and SM schemes and examine their ability to reproduce characteristic polarimetric signatures commonly found in polarimetric radar observations. The TM simulation is not investigated here, based on the similarity between the DM and TM simulations of Dawson (2009) and Dawson et al. (2010), but can be explored in future studies. Radial velocity is included in our emulator but not discussed in this paper, as we focus only on the polarimetric signatures.

This paper is organized as follows: in section 2, we discuss the polarimetric radar simulator and assumptions about the DSDs. In section 3, the numerical simulation of the supercell storm is described. In section 4, we present the polarimetric radar simulations and the associated polarimetric signatures and compare them with the results using an SM scheme. The results are summarized in section 5.

2. Polarimetric radar data simulator

The simulator developed in this study is more complex and general than the one reported in JZX08. As discussed in JZX08, the DSD-related parameters within the simulator should be consistent with those used in the numerical model. Within the multimoment microphysics scheme of Milbrandt and Yau (2005a,b) used in this study and Dawson (2009), the DSDs of each species, $n(D)$, are modeled by a gamma distribution that contains three free parameters,

$$n(D) = N_0 D^{\alpha} e^{-\Lambda D}, \tag{1}$$

where D is the particle or drop diameter, and N_0, α, and Λ are the intercept, shape, and slope parameters, respectively. In brief, many SM schemes used in operational systems assume a Marshall and Palmer (1948) distribution with $\alpha = 0$ and a fixed N_0, which is an inverse exponential distribution. The predicted variable, hydrometeor mixing ratio q, monotonically determines Λ and thus $n(D)$. On the other hand, the DM scheme used in this study predicts q and the total number of particles N_t, which allows for the independent change of N_0 and Λ while α is fixed. Researchers reported that N_0 can vary significantly among precipitation systems and even within the same system (e.g., Waldvogel 1974; Gilmore et al. 2004). Therefore, the DM scheme may be more appropriate for the simulation of precipitation systems. The TM scheme usually predicts q, N_t, and the radar reflectivity factor Z. All three DSD parameters—N_0, Λ, and α—vary freely in time and space, and the width of the DSD can practically vary over a wide range with the TM scheme. For more detailed information on the various microphysical parameterizations, the reader is referred to Milbrandt and Yau (2005a) and Dawson et al. (2010).

In the simulator, fixed densities of 1000, 100, and 913 kg m^{-3} are assumed for rain (ρ_r), snow (ρ_s), and hail (ρ_h), respectively, as in the prediction model. Additional particle characteristics are needed to simulate polarimetric variables, such as the shape, the statistical properties of the particle orientation, and the ice–water composition of the hydrometeors. Since these parameters are not explicitly specified in the prediction model, assumptions have to be made, based on as much available information as possible. The assumptions we make here are largely inherited from JZX08. Briefly, raindrops, snow aggregates, and hailstones are all assumed as oblate spheroids falling with the major axis aligned horizontally. The oblateness depends on the size of a raindrop while a fixed axis ratio of 0.75 is assumed for snow aggregate and hailstone. [Other axis ratios for hailstones, such as the one based on the Oklahoma hailstorms studied by Knight (1986), are also available as options in the radar simulator.] The mean canting angles of all hydrometeor types are assumed to be 0°. The standard deviation (SD) of the canting angle is assumed to be 0° for raindrops, 20° for snow aggregates, and a function of the water content in melting hail with maximum 60° for dry hailstones. For more detailed information, the reader is referred to JZX08.

To benefit from the T-matrix scattering calculations, which do not allow for analytical integration, we carry out a numerical integration of the scattering amplitudes over the DSD for all hydrometeor types in the simulator. This allows us to deploy the revised axis ratio relation

based on the observations for rain (Brandes et al. 2002), which yields more spherical shapes consistently at all sizes when compared with that given in Zhang et al. (2001),

$$r = 0.9951 + 0.025\,10D - 0.036\,44D^2 + 0.005\,303D^3 - 0.000\,249\,2D^4. \quad (2)$$

While a few other relationships, including the ones given by Green (1975) and Beard et al. (1991), are available in the simulator as alternative user-selectable options, new relationships can easily be added as well.

Within the scattering calculations, the maximum sizes of rain drops ($D_{\max,r}$), snow aggregates ($D_{\max,s}$), and hailstones ($D_{\max,h}$) are assumed to be 8, 30, and 70 mm, respectively. These size ranges are partitioned into 100 bins. For rain, dry snow, and dry hail, the forward and backward scattering amplitudes along the major and minor axes with assumed drop shape are calculated at the center of each size bin and stored in lookup tables. For melting species, lookup tables are constructed at uniform water fraction intervals, which is 5% in this study. The same melting ice and dielectric constant models developed in JZX08 are employed in the scattering calculation. For example, for a melting snow aggregate with a specified water fraction, the density and dielectric constant of that particle are calculated and used to compute the forward and backward scattering amplitudes at each size bin with that water fraction. These scattering amplitudes are then integrated over the DSD when the model mixing ratios (and the total number concentration for DM and the additional sixth moment of DSD for TM schemes) are given as input.

We employ formulations for radar reflectivity factors at horizontal and vertical polarizations that are more exact than those in JZX08 by including the complex scattering amplitude in the calculations as follows (Zhang et al. 2001):

$$Z_{h,x} = \frac{4\lambda^4}{\pi^4 |K_w|^2} \int_0^{D_{\max,x}} \{A|f_{a,x}(\pi)|^2 + B|f_{b,x}(\pi)|^2 + 2C\,\mathrm{Re}[f_{a,x}(\pi) f_{b,x}^*(\pi)]\} n(D)\,dD \ (\mathrm{mm^6\,m^{-3}}) \quad (3)$$

and

$$Z_{v,x} = \frac{4\lambda^4}{\pi^4 |K_w|^2} \int_0^{D_{\max,x}} \{B|f_{a,x}(\pi)|^2 + A|f_{b,x}(\pi)|^2 + 2C\,\mathrm{Re}[f_{a,x}(\pi) f_{b,x}^*(\pi)]\} n(D)\,dD \ (\mathrm{mm^6\,m^{-3}}), \quad (4)$$

where

$$A = \langle \cos^4\phi \rangle = \frac{1}{8}(3 + 4\cos 2\overline{\phi} e^{-2\sigma^2} + \cos 4\overline{\phi} e^{-8\sigma^2}),$$

$$B = \langle \sin^4\phi \rangle = \frac{1}{8}(3 - 4\cos 2\overline{\phi} e^{-2\sigma^2} + \cos 4\overline{\phi} e^{-8\sigma^2}),$$

and

$$C = \langle \sin^2\phi \cos^2\phi \rangle = \frac{1}{8}(1 - \cos 4\overline{\phi} e^{-8\sigma^2}),$$

and subscript x can be r (for rain) or rs (for rain–snow mixture), ds (for dry snow), rh (for rain–hail mixture), or dh (for dry hail). Here, $f_a(\pi)$ and $f_b(\pi)$ are complex backscattering amplitudes for polarizations along the major and minor axes, respectively, and f_a^* and f_b^* are their respective conjugates. Here, Re[$\cdots$] represents the real part of the complex number, and $|\cdots|$ means the magnitude of the value between single bars; $\langle \cdots \rangle$ means that an ensemble average is taken over canting angles, and $n(D)$ defines the DSD and is the number of particles per unit volume of air and unit bin size. Truncation is applied at maximum sizes of raindrop, snow aggregates, and hailstone when integration over DSD is performed. The mean canting angle is $\overline{\phi}$, the standard deviation of the canting angle is σ, the radar wavelength is λ, and the dielectric factor for water is $K_w = 0.93$.

The same equations for logarithmic reflectivity at horizontal and vertical polarizations and differential reflectivity of JZX08 are used here [see their Eqs. (14)–(16), respectively]. The value Z_{DR} is a good indicator of the mean shape of hydrometeors and depends on their relative orientation to the radar beam. Therefore, DSD changes toward larger or smaller drop sizes can be roughly inferred from the Z_{DR} value.

The specific differential phase is defined as

$$K_{\mathrm{DP},x} = \frac{180\lambda}{\pi} \int_0^{D_{\max,x}} C_k\,\mathrm{Re}[f_{a,x}(0) - f_{b,x}(0)] n(D)\,dD \ (^\circ\,\mathrm{km^{-1}}), \quad (5)$$

where $C_k = \langle \cos 2\phi \rangle = \cos 2\overline{\phi} e^{-2\sigma^2}$. Note that $f_a(0)$ and $f_b(0)$ here are forward scattering amplitudes for polarizations along the major and minor axes, respectively. The $K_{\rm DP}$ is regarded as more useful in quantitative precipitation estimation because it is more linearly proportional to the rainfall rate than reflectivity. However, the $K_{\rm DP}$ field is often very noisy in weak rain regions and is vulnerable to errors.

The cross-correlation coefficient (Ryzhkov 2001; Jung 2008, hereinafter J08) is defined as

$$\rho_{hv} = \frac{|Z_{hv,r} + Z_{hv,\rm ds} + Z_{hv,\rm dh} + Z_{hv,\rm rs} + Z_{hv,\rm rh}|}{[(Z_{h,r} + Z_{h,\rm ds} + Z_{h,\rm dh} + Z_{h,\rm rs} + Z_{h,\rm rh})(Z_{v,r} + Z_{v,\rm ds} + Z_{v,\rm dh} + Z_{v,\rm rs} + Z_{v,\rm rh})]^{1/2}}, \tag{6}$$

where the numerator is given as a product of two orthogonal copolar components of the radar signals and computed as

$$Z_{hv,x} = \frac{4\lambda^4}{\pi^4 |K_w|^2} \int_0^{D_{\max,x}} \{C[|f_{a,x}(\pi)|^2 + |f_{b,x}(\pi)|^2] + A[f_{a,x}(\pi) f^*_{b,x}(\pi)] + B[f_{b,x}(\pi) f^*_{a,x}(\pi)]\} n(D)\, dD \ (\mathrm{mm}^6\, \mathrm{m}^{-3}). \tag{7}$$

Cross-correlation coefficient ρ_{hv} is very useful in detecting the melting layer since it is sensitive to the presence of randomly oriented wet ice particles; ρ_{hv} is very high for pure rain and relatively high for low-density dry ice particles, but is much lower in the presence of large, wet hailstones. The simpler versions of Eqs. (3), (4), and (7) can be found in J08, where the empirical coefficient $\rho_{0,x}$, which is less than unity, is introduced in the second and third terms within the integral of Eq. (7) to better fit the observed ρ_{hv} range, and Rayleigh assumptions are employed for snow aggregate and hailstones for efficiency.

When creating observations on the radar elevation planes, the effective earth radius model (Doviak and Zrnic 1993) is used to take into account beam bending, and a Gaussian beam weighting function described in Xue et al. (2006) is used in the vertical direction. The error model described in Xue et al. (2007) and Jung et al. (2008b, hereinafter JXZS08) is optional for adding simulated observation errors. In this study, error-free polarimetric variables are created at each grid point.

3. Numerical simulation

Similar to the truth simulation used in JXZS08, an idealized supercell storm is initialized by a thermal bubble placed in a horizontally homogeneous environment defined by the sounding of the 20 May 1977 Del City, Oklahoma, supercell storm (Ray et al. 1981). The storm is simulated using the Advanced Regional Prediction System (ARPS; Xue et al. 2000, 2001, 2003), which is a fully compressible and nonhydrostatic atmospheric prediction model. The MM schemes described in Milbrandt and Yau (2005a,b) have been implemented recently in ARPS (Dawson et al. 2007; Dawson 2009) and are used in this study. This Milbrandt–Yau scheme is referred to as MY05 hereinafter.

With the DM option of the MY05, the ARPS predicts three velocity components u, v, and w; potential temperature θ; pressure p; mixing ratio of water vapor q_v; mixing ratios of cloud water, rainwater, cloud ice, snow aggregate, and hail (q_c, q_r, q_i, q_s, and q_h, respectively); and their total number concentrations (Nt_c, Nt_r, Nt_i, Nt_s, and Nt_h, respectively). The graupel category originally included in the MY05 package is turned off to maintain consistency with our previous experiments (JXZS08 and JZX08). The turbulent kinetic energy is also predicted by the model and is used in the 1.5-order subgrid-scale turbulence closure scheme.

The initiating bubble has an ellipsoidal shape and has 4-K maximum temperature perturbation, is 10 km long and 1.5 km high in radius, and is centered at $x = 48$ km, $y = 48$ km, and $z = 1.5$ km in a $158 \times 128 \times 16$ km^3 model domain. Radiation, rigid wall with a wave-absorbing layer, and free-slip condition are applied to the lateral, top, and bottom boundaries, respectively.

A few changes are made to the configurations used in JXZS08 and JZX08 to accommodate the use of the DM scheme. Following Dawson et al. (2010), the smaller horizontal grid spacing of 1.0 km is used with the vertical grid spacing of 0.5 km. Constant winds of $u = 1$ m s^{-1} and $v = 13$ m s^{-1} are subtracted from the original sounding to keep the storm near the center of the domain. A fourth-order monotonic computational mixing (Xue 2000) is used to prevent the Gibbs phenomenon.

The MM scheme of MY05 assumes that each hydrometeor type has a constant density. The default values for rain, snow, and hail are 1000, 100, and 913 kg m^{-3} but

can be altered by the user. The DSDs for all hydrometeor types are modeled by exponential distribution in the current study, by assuming the shape parameters for each species to be 0; doing so maintains a consistency with the DSDs used in the SM runs.

4. Simulated polarimetric signatures

a. Storm evolution and simulated reflectivity

Figure 1 shows the time evolution of the reflectivity and other fields of the simulated supercell storm using SM and DM microphysics schemes of MY05, at 250-m altitude, where the first scalar model level above ground is found. Briefly, the updraft quickly intensifies during the first 20 min, with a reflectivity core greater than 40 dBZ appearing after 10 min of simulation (not shown). While the forward flank regions continue to expand in the next 30 min, the storm splits into two cells at around 1 h (Fig. 1b). The left-moving cell (relative to the environmental shear vector) then continues to develop while propagating to the northwest of the right-moving cell. The right-moving cell is at its mature stage by 80 min of model time and maintains its intensity for the next few hours. In this study, we focus on the right-moving storm, which is usually the dominant one.

As discussed in Dawson et al. (2007, 2010) and Dawson (2009), though for a different case, the simulated reflectivity using the DM scheme (Figs. 1b,d,f) shows a more realistic structure and intensity in the hook echo and forward flank regions compared to the results of the SM scheme (Figs. 1a,c,e). Our simulated storm using the MY05 SM scheme is very similar to that using the Lin et al. (1983) ice microphysics scheme shown in Fig. 2 of Tong and Xue (2005), which used the same Del City sounding. Compared to the simulated reflectivity obtained with the DM scheme, that using the SM scheme has a kidney shape with a narrow forward flank, while DM produces a swirl-shaped weak echo region (WER) wrapping around the hook echo and extends the forward flank to the far east of the storm (Figs. 1b,d,f). Another significant difference between the storms using the SM and DM schemes is in the cold pool strength. SM schemes with default DSD parameter settings tend to produce stronger cold pools than DM schemes. Dawson et al. (2010) showed that one of the main causes of the strong cold pool with SM schemes is the stronger evaporative cooling of raindrops in the downdraft related to the fixed, large, N_{0r}, which corresponds to a larger number of small drops that can evaporate quickly.

A detailed evaluation of microphysics schemes is beyond the scope of this study. Our focus will be on the ability of our simulator in reproducing characteristic polarimetric signatures when using different microphysics schemes.

b. Simulated polarimetric radar variables

Several unique polarimetric signatures have been reported in observational studies of supercell storms. They include strong Z_{DR} and K_{DP} columns, a midlevel Z_{DR} ring, a hail signature (Z_{DR} hole), Z_{DR} arc (Z_{DR} shield), midlevel ρ_{hv} ring, and K_{DP} foot (e.g., Wakimoto and Bringi 1988; Bringi et al. 1986; Hubbert et al. 1998; KR08; KR09; Romine et al. 2008). These signatures appear in the specific locations within a storm as a result of storm dynamics and microphysics. If the numerical model can handle the related storm dynamics and microphysics properly, a realistic polarimetric radar simulator should be able to reproduce those signatures. In this study, the ability of the SM and DM schemes in reproducing individual signatures is examined using our simulator in the following subsections.

1) Z_{DR} AND K_{DP} COLUMNS

Figure 2 shows the vertical structures of Z_H, Z_{DR}, and K_{DP} (Figs. 2a,b,c, respectively) along line AA′ in Fig. 1f. This cross section passes through the vicinity of the maximum vertical velocity. The melting layer is elevated within a deep reflectivity core at the convection region near $x = 58$ km (Fig. 2a). The locations of the Z_{DR} and K_{DP} columns are associated with the updraft (Figs. 2b,c). Observational studies suggest that the Z_{DR} column is associated with supercooled rainwater carried aloft by a strong updraft (Illingworth et al. 1987; Conway and Zrnic 1993) while the shed raindrops from the wet hail near the updraft are presumed to be responsible for the K_{DP} column (Hubbert et al. 1998; Loney et al. 2002). The Z_{DR} and K_{DP} columns extending above the 0°C level near the updraft core are evident in Fig. 2. As reported in the observational study of Ryzhkov et al. (2005) and in Romine et al. (2008), the K_{DP} column is connected to the K_{DP} foot in the rear-flank downdraft (RFD) region near the surface (Figs. 2c, 10). These columns are qualitatively similar to those shown in Figs. 6 and 7 of KR08.

An offset in the centers of the K_{DP} and Z_{DR} columns was pointed out by Loney et al. (2002) and KR08 in their observational studies of polarimetric signatures. In the observations, the K_{DP} column often is found west or northwest of the Z_{DR} column. A similar offset is observed in the lower midlevels (Figs. 3a,d) in our simulation, while they become collocated at the upper midlevels (Figs. 3c,f). At the 3-km altitude, the Z_{DR} column is located southeast of the updraft core near the reflectivity hook. This agrees well with the location of the Z_{DR} column reported in Hubbert et al. (1998). At this level, the

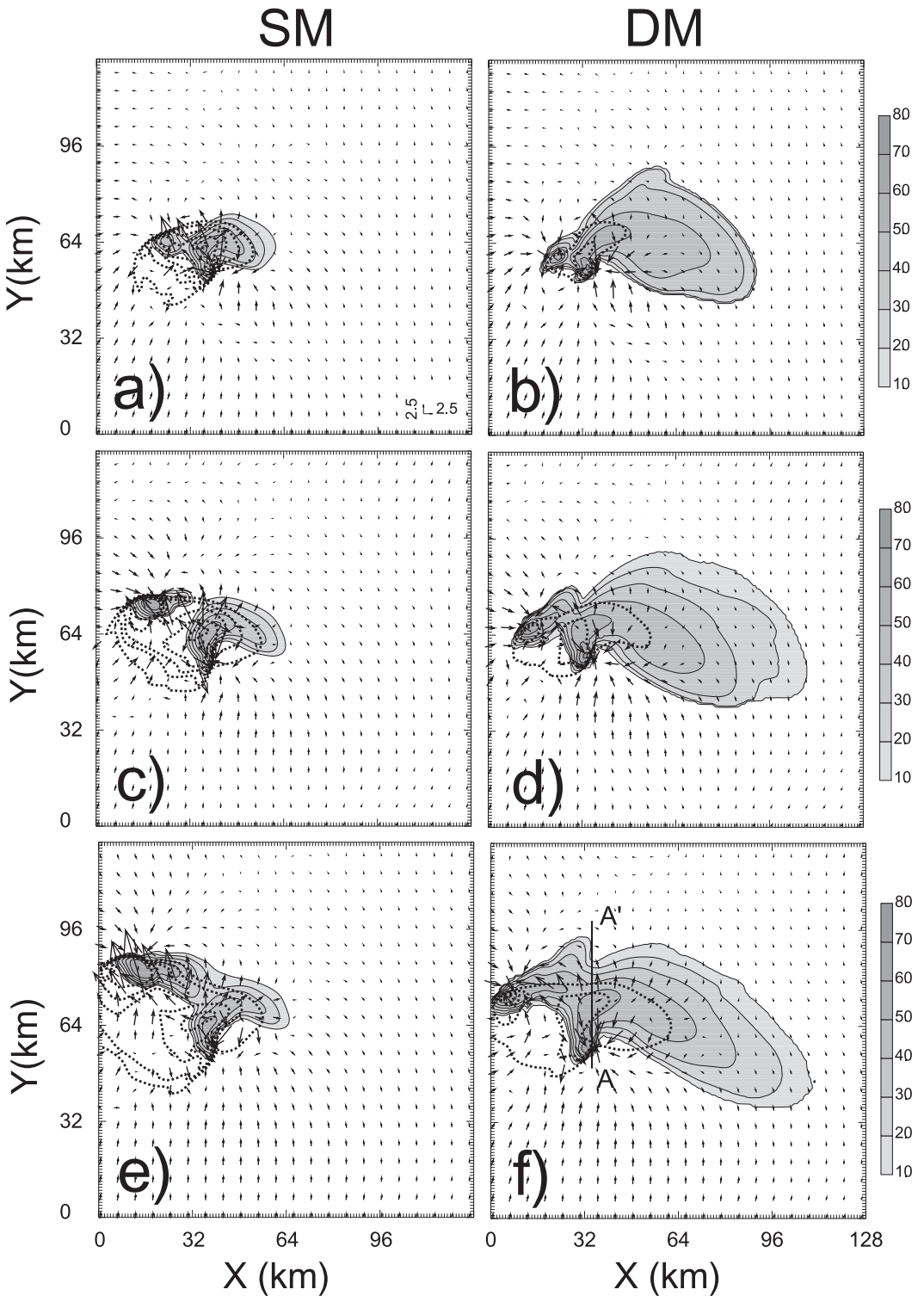

FIG. 1. Reflectivity (thin solid contours and shading), negative perturbation potential temperature (dotted contours at 1.0-K intervals from −1.0 K) and horizontal perturbation wind vectors (plotted every sixth grid point; m s^{-1}) at z = 250 m for the simulated storm using (left) SM and (right) DM microphysics schemes at (a),(b) 60, (c),(d) 80, and (e),(f) 100 min. Line AA′ in (f) show the locations of the vertical cross sections to be shown in Fig. 2.

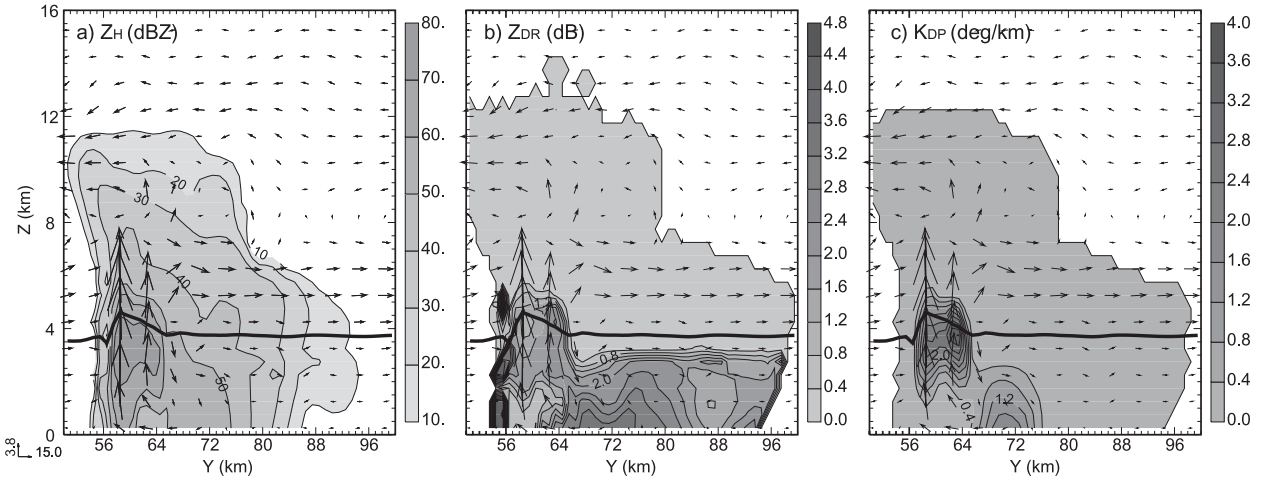

FIG. 2. Vertical cross sections of simulated (a) Z_H (dBZ), (b) Z_{DR} (dB), and (c) K_{DP} (° km^{-1}), along line AA′ shown in Fig. 1h corresponding to $x = 34.5$ km of the simulated supercell storm at 100 min. The 0°C isotherms are shown as thick black lines. Deep vertical columns with high Z_{DR} and K_{DP} values are extended above freezing level at this cross section.

K_{DP} column is found at the reflectivity maximum and in the west and northwest part of the updraft core. At the 4-km altitude, the Z_{DR} column appears as a half-ring wrapping around the updraft core on the east side (Fig. 3b), while the center of the K_{DP} column is moving toward the updraft core (Fig. 3e). At the 5-km height, the Z_{DR} and K_{DP} columns are almost collocated with the updraft core (Figs. 3c,f). No obvious offset in the centers is found in the SM run (Fig. 4).

The main cause of the offset of the Z_{DR} column from the updraft core is the presence of hail. From Figs. 3g–i, the production of q_r apparently is strongly related to the updraft. Within the updraft, the low-level q_r is transported to the higher level, and q_r is also created through in situ condensation and autoconversion from cloud water; q_h is also produced in the updraft. Large hailstones fall through the updraft, and small hailstones are carried out of the updraft while growing and falling in the forward flank region north of the updraft core. The high-q_h region overlaps with the high q_r region in the west-northwest. The presence of hail reduces the Z_{DR} because the tumbling nature of the hailstones makes their apparent shape close to spherical. Therefore, the high Z_{DR} column shows up at the southeast-to east-side of the updraft.

On the other hand, the K_{DP} is almost transparent to the hail and is sensitive only to the amount of rainwater. Therefore, the K_{DP} maximum, high q_r region, and updraft core are almost collocated.

2) Z_{DR} ARC

The Z_{DR} arc is the low-level signature often observed at the southern edge of forward flank along the sharp gradient zone of reflectivity in right-moving supercells (Ryzhkov et al. 2005; KR08; KR09; Romine et al. 2008). This is characterized by a horizontally elongated high Z_{DR} band along the right edge of the forward flank near the surface and is a quite common feature in supercells, regardless of season or geographic region. Disdrometer and polarimetric radar measurements of Schuur et al. (2001) showed that a very large median volume diameter is observed in this region. This signature was analyzed in detail in KR09, where the researchers argued that the size sorting mechanism, because of strong wind speed and directional shears, is primarily responsible for this signature; large drops discharged from the updraft fall into the region close to the origin, while smaller drops are advected farther into the forward flank. The rain evaporation is likely another contributing factor modifying the DSD toward a large D_{nr} because it selectively depletes small drops more quickly than larger drops (Rosenfeld and Ulbrich 2003). At the location of the Z_{DR} arc, the DSD, initially lacking small drops, loses small drops fast because of evaporation while falling through dry air in a shear environment (Milbrandt and Yau 2005a; Dawson et al. 2010). To properly model such processes responsible for DSD changes, a two- or higher-moment microphysics scheme must be used; an SM scheme is not capable of handling such mechanisms (Fig. 5a).

The modified DSD of rain as a result of the size sorting can be evaluated easily by examining the mean-mass diameter D_{nr}, where D_{nr} is calculated for the exponential distribution as

$$D_{nr} = \left(\frac{q_r \rho_{air}}{\pi \rho_r \mathrm{Nt}_r}\right)^{1/3}, \tag{8}$$

where ρ_{air} is the density of air. For an SM scheme, D_{nr} is dependent only on q_r because $\mathrm{Nt}_r = N_{0r} D_{nr}$, where N_{0r} is

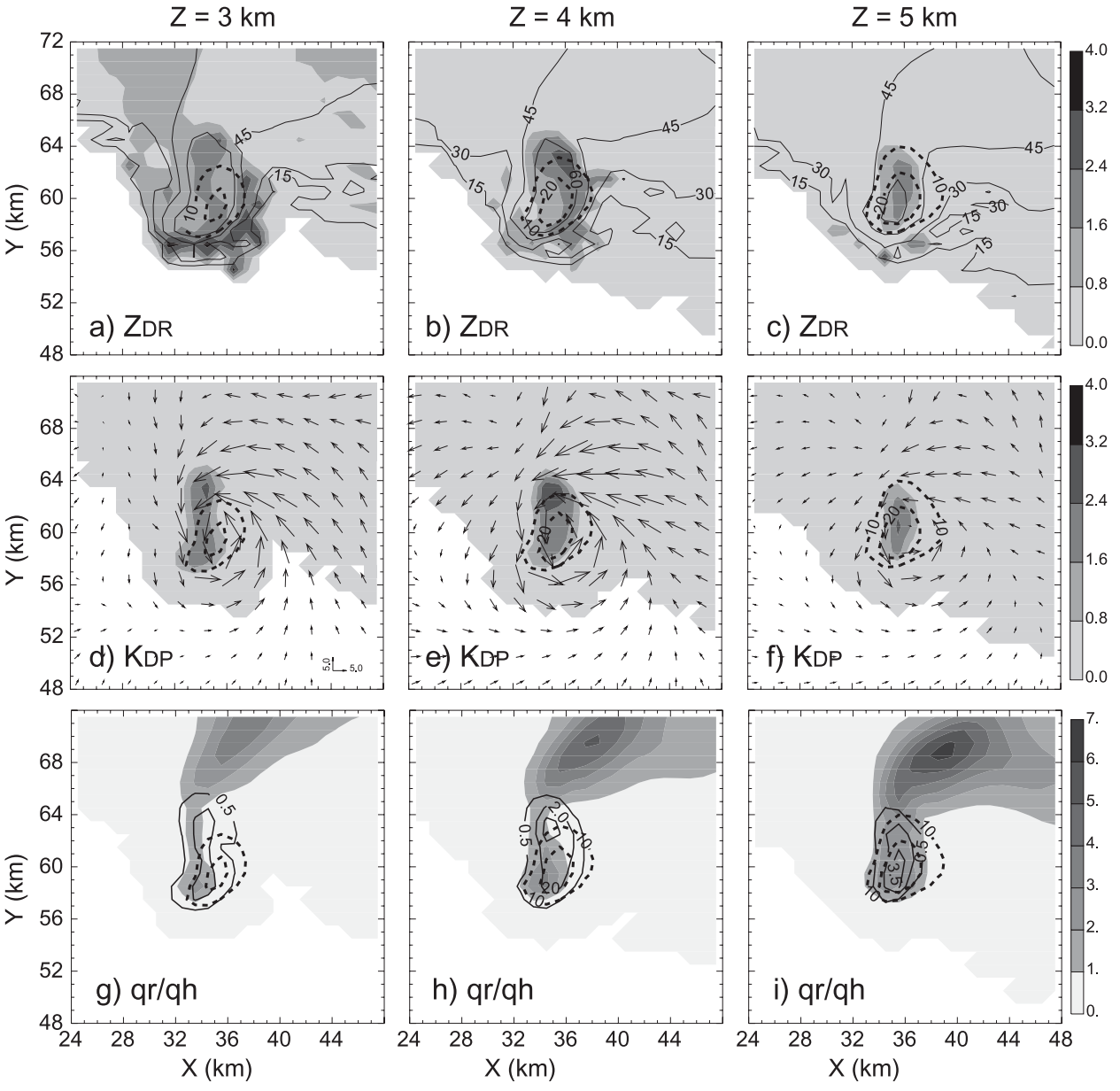

FIG. 3. (a)–(c) Z_{DR} (shading; dB) and reflectivity (solid contours at 15-dBZ intervals, starting at 15 dBZ), (d)–(f) K_{DP} (shading; ° km^{-1}) and perturbation horizontal wind vectors (plotted every other grid point; m s^{-1}), and (g)–(i) hail mixing ratio q_h (shading; g kg^{-1}) and rain mixing ratio q_r (solid contours at 1.5 g kg^{-1} intervals starting at 0.5 g kg^{-1}) at (left) 3-, (center) 4-, and (right) 5-km height, at 100 min of simulated storm. The vertical velocity contours (dotted contours at 10 m s^{-1} intervals starting at 10 m s^{-1}) are overlaid on each plot.

a constant. The DSD directly affects Z_{DR} because Z_{DR} is proportional to the median diameter of precipitation particles in the radar resolution volume. The calculated D_{nr} for SM and DM is presented in Fig. 5 along with simulated Z_{DR}.

The Z_{DR} arc signature is well captured by the DM scheme and polarimetric radar data simulator at a 0.5-km altitude at 80 min of simulated storm in Fig. 5b. The high Z_{DR} region along the southern edge of the forward flank is shallow (~2 km deep), rather narrow, but persistent in time, quantitatively similar to polarimetric radar observations of supercell storms, and it shifts slightly toward the north with height. The arc band becomes weak and broad above 2 km, practically fading away. The shape and location of the high Z_{DR} region match the D_{nr} pattern. The q_r pattern, in conjunction with that of D_{nr}, designates this area as having a small number of large drops and lacking small drops. On the other hand, the

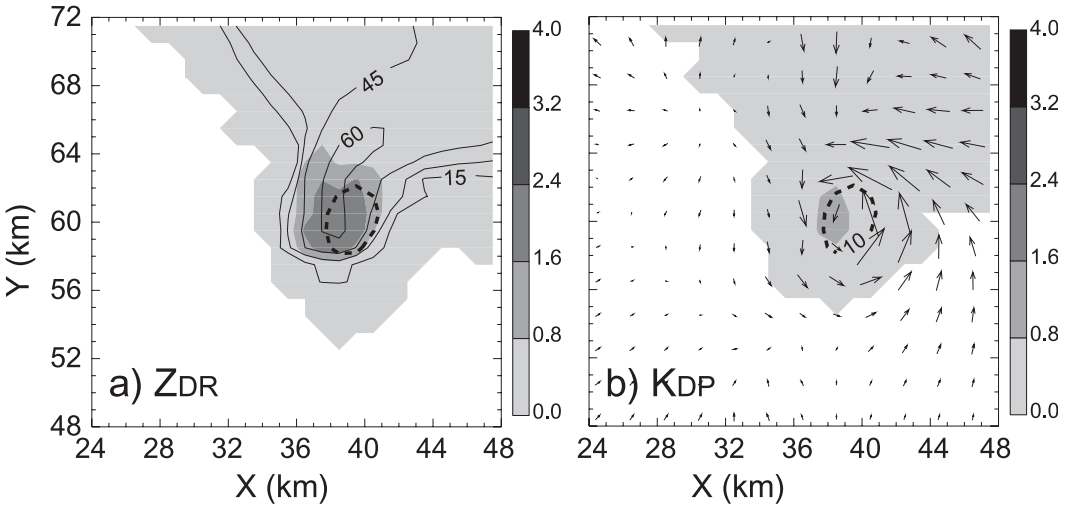

FIG. 4. (a) As in Fig. 3a and (b) as in Fig. 3d for the SM scheme.

simulated storm using the SM scheme completely misses the Z_{DR} arc signature because both D_{nr} and Z_{DR} are proportional only to rainwater mixing ratio q_r (Fig. 5a).

3) MIDLEVEL Z_{DR} AND ρ_{hv} RINGS

The midlevel Z_{DR} ring (KR08) refers to the enhanced Z_{DR} in the shape of a ring occasionally found in the middle levels. The Z_{DR} ring is sometimes a complete circle and sometimes just a half-ring. KR08 reported that the enhanced Z_{DR} region is found always on the right flank of the updraft when only a half-ring is manifested. In our simulation, it is usually a half-ring on the right flank of the updraft at the midlevels and close to a complete ring in the lower levels.

The half-Z_{DR} ring in Fig. 6b mostly overlaps with the high D_{nr} region. The maximum D_{nr} region is collocated with the updraft core. The local maxima found on the south and east sides of the main D_{nr} core may be explained by large raindrops falling around the updraft following a cyclonic circulation (associated with a cyclonically rotating updraft; Figs. 3d–f). The missing half of the ring signature is closely related to the presence of hail (Fig. 6b). As discussed earlier in section 4b(1), the presence of hailstones reduces the Z_{DR} values because their tumbling motion and random orientation make their apparent shape spherical to radar beams. At the 4-km altitude, the region with high–hail mixing ratios is located to the west and northwest of the updraft core. This weakens the Z_{DR} signature on the left flank of the updraft.

The ρ_{hv} ring is another midlevel feature with depressed (instead of increased) ρ_{hv} values in a ring pattern (KR08). A well-defined ρ_{hv} ring is seen in Fig. 6d. The ρ_{hv} values for pure water and ice are very high but decrease when hydrometeors of diverse types are mixed together. The dotted contours in Fig. 6d show the ratio of rain–hail mixture to the rain and dry hail total mixing ratio. High values of this ratio indicate the presence of three different types, with the mixture being dominant in the regions of the ρ_{hv} ring. The low values of the ratio suggest either pure rain or dry hail is dominant [see Eq. (2) and section 3b of JZX08 for more details on the melting ice model used here]. The pattern of this ratio agrees well with the ring-shaped ρ_{hv} depression. These midlevel Z_{DR} and ρ_{hv} rings are very weak or completely missing when an SM is used (Figs. 6a,c). The D_{nr} contours are not shown in Fig. 6a because the maximum D_{nr} is smaller than 1.2 mm because of the large intercept parameter value with SM schemes.

When ice is in a melting phase, the resonance effect due to Mie scattering can contribute to the reduction of ρ_{hv} (Fig. 7a), which occurs when the ratio $D|\varepsilon|^{1/2}/\lambda$ approaches 1 (KR08; KR09), where ε is the dielectric constant. For dry hail, ρ_{hv} slowly decreases with size within the range shown in Fig. 7a, in which the particle size is truncated at 42.35 mm. With the given exponential DSD, large drops have little effect because the number of drops is very small at that size, although the resonance effect can be much more significant in very large drops. The ρ_{hv} shows a sudden drop at a certain size. Both the characteristic size and maximum amplitude reduction decrease with increasing water fraction. The size sorting mechanism is also necessary to simulate this signature, so that the DSD can have a sufficient number of hailstones at the characteristic size to reduce the total ρ_{hv} values.

Figure 7b shows the number concentration $N(D)$ at each particle size D and accumulated ρ_{hv} from the minimum size up to size D for two selected grid points from the simulated storm shown in Figs. 6b and 6d. The rain–hail

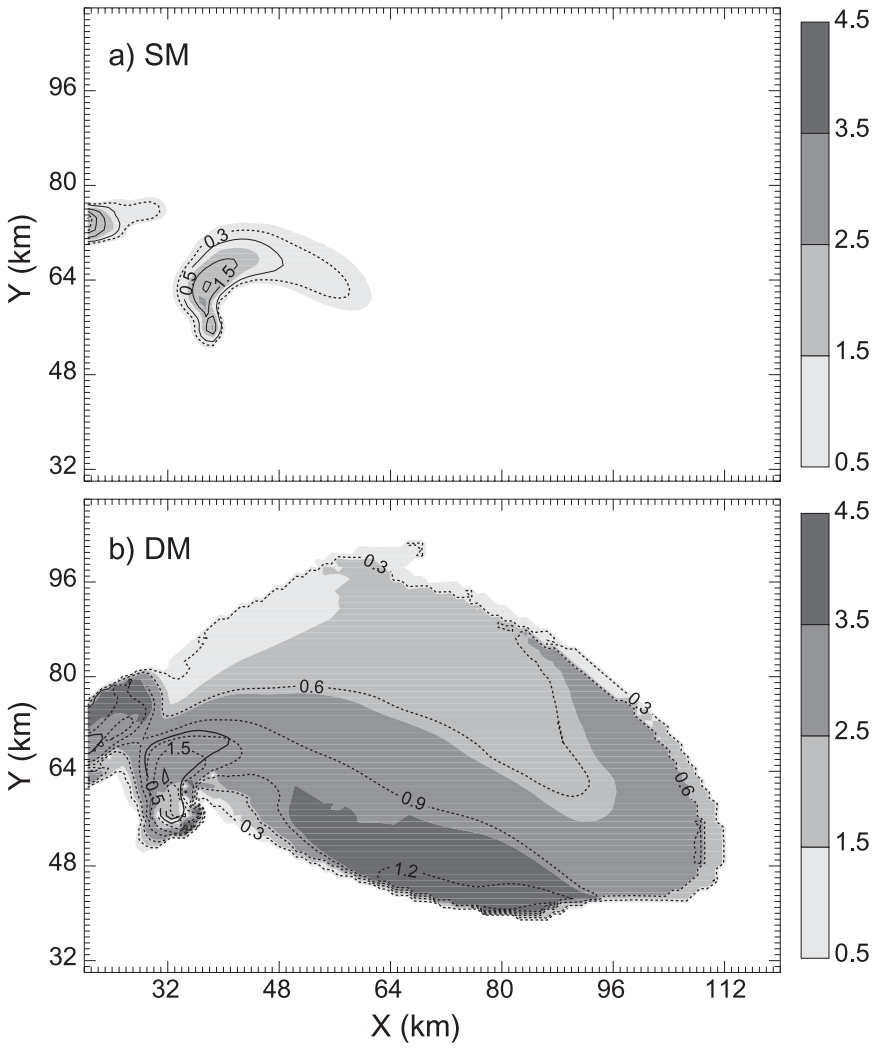

FIG. 5. The Z_{DR} (shading), q_r (solid contours at 1.0 g kg^{-1} intervals, starting at 0.5 g kg^{-1}), and mean-mass diameter of raindrops D_{nr} (dotted black contours at intervals of 0.3 mm, starting at 0.3 mm) for the (a) SM and (b) DM scheme at $z = 500$ m at 80 min of simulated storm. The Z_{DR} arc structure in the southern edge of the forward flank region agrees well with the area of the large mean-mass diameter with the DM scheme.

mixture mixing ratio, percentage water fraction, intercept parameter, and total number concentration for these two grid points are (1.03 g kg^{-1}, 51%, 1.49 $\times$ 10^4 m^{-4}, 33.893 m^{-3}) and (0.995 g kg^{-1}, 46%, 1.95 $\times$ 10^5 m^{-4}, 208.42 m^{-3}). Mixing ratios are similar at these two points but their intercept parameters differ by an order of magnitude. When the intercept parameter is large, $N(D)$ decreases rapidly with size (thick solid gray) and particles with resonance sizes have very little impact on accumulated ρ_{hv} (thick dashed gray). On the contrary, $N(D)$ decreases slowly when the intercept parameter is small (solid black) and accumulated ρ_{hv} exhibits a sudden reduction near the resonance sizes and slowly increases as D further increases (dashed black).

We would like to point out that the simulated ρ_{hv} is higher than the typically observed values. One source of difference might be the simplified model of randomly orientated spheroids for hail and snow used here, which does not account for the effect of irregular shapes of natural hydrometeors. The high ρ_{hv} also may be attributed partially to our treating each precipitating type independently when calculating radar reflectivity factor and combining them afterward [see Eq. (6)] while in the real atmosphere the radar would see them as a mixture of irregular shaped, randomly oriented particles. Nonmeteorological effects that can also contribute to the reduction of ρ_{hv}, such as noise bias, clutter contamination, dust, and bugs, are not included in our simulator.

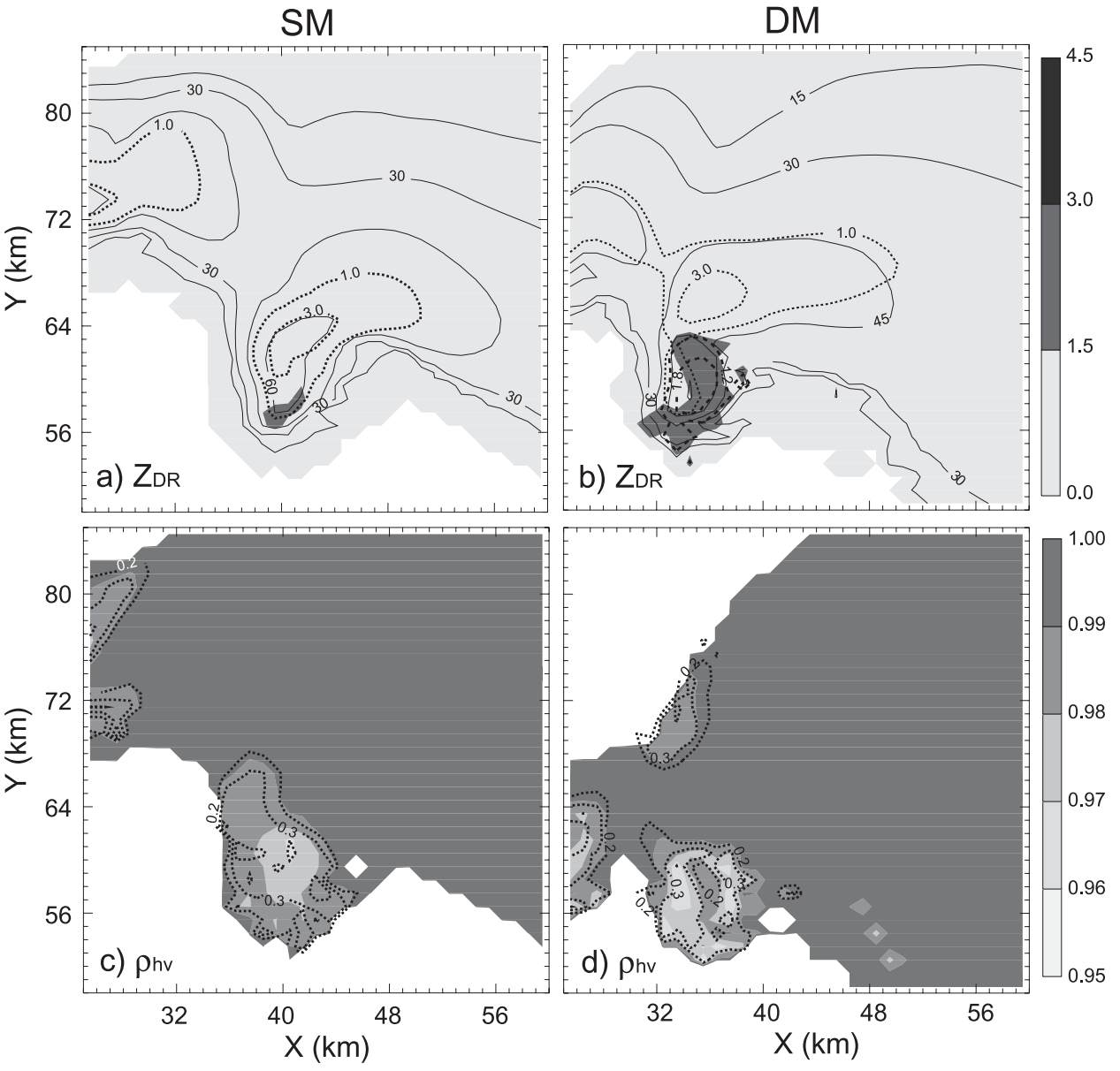

FIG. 6. (a),(b) Z_{DR} (shading), Z_H (solid contours at 15-dBZ intervals from 15 dBZ), q_h (dotted contours at 2.0 g kg^{-1} intervals from 1.0 g kg^{-1}), and D_{nr} (thick dashed contours at intervals of 0.6 mm, starting at 1.2 mm), and (c),(d) ρ_{hv} (shading) and the ratio of rain–hail mixture to the sum of rain and dry hail mixing ratios (dotted contours at 0.1 intervals from 0.2) for the (left) SM and (right) DM scheme at 80 min at $z = 4$ km. Ring features are prominent at this level.

These may partially be responsible for the rather high ρ_{hv} in our simulation.

To further evaluate the fidelity of our simulator, we compared the above signatures to those simulated using the simple simulator developed in J08, where efficiency was given a high priority when it was developed for data assimilation purposes. The simulator of J08 is found to be able to simulate most of the signatures except for the ρ_{hv} ring with the DM scheme. The Z_{DR} and K_{DP} values are somewhat higher than those using a new simulator because of the choice of the axis ratio there to avoid numerical integration. The ρ_{hv} ring could not be simulated correctly because Mie scattering for the ice species is not included there (Fig. 8).

4) HAIL SIGNATURE IN FORWARD FLANK DOWNDRAFT

The observed hail signature is characterized by a high Z_H and low Z_{DR} at the lowest radar elevation associated with hail reaching the ground (KR08). This feature is also

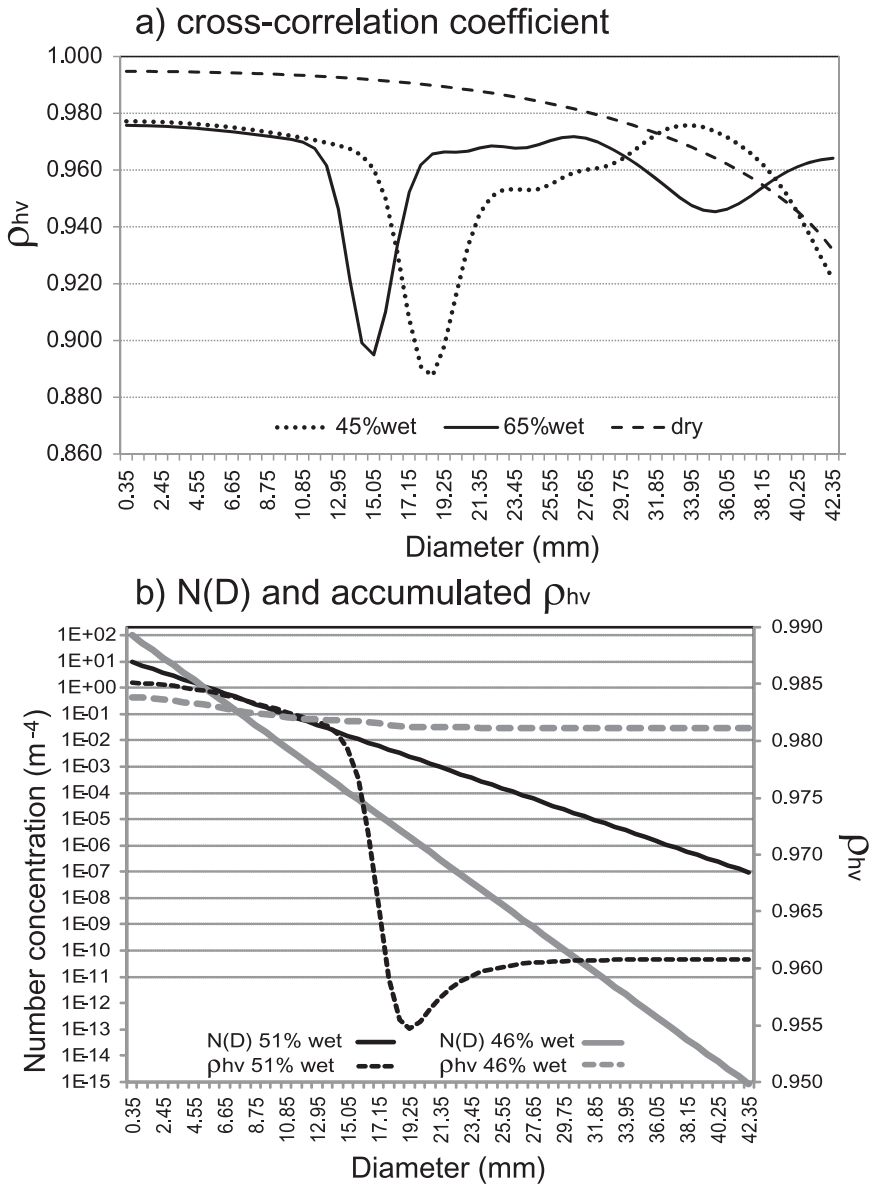

FIG. 7. (a) Simulated ρ_{hv} with size of melting hailstones for the fraction of water, $f_w = 0.45$ (dotted), 0.65 (solid), and dry hailstone (dashed). (b) The number concentration $N(D)$ (solid) and accumulated ρ_{hv} (dashed) for two selected grid points from the simulated storm shown in Fig. 5 with (the rain–hail mixture mixing ratio, percent fraction of water, intercept parameter, and total number concentration) = (1.03 g kg^{-1}, 51%, 1.49×10^4 m^{-4}, 33.893 m^{-3}; black) and (0.995 g kg^{-1}, 46%, 1.95×10^5 m^{-4}, 208.42 m^{-3}; thick gray).

called "Z_{DR} hole" (Wakimoto and Bringi 1988), which often stretches from the surface up to a certain height. Our simulated storm exhibits depressed Z_{DR} hole surrounded by high Z_{DR} values at the 500-m altitude, where high hail concentration is present (Fig. 9b). The simulated Z_{DR} pattern at this altitude is substantially similar to the observations shown in Fig. 3a of KR08. This hail signature is also shown in the SM run although it is weak and its location is shifted to the north (Fig. 9a).

5) K_{DP} FOOT

The K_{DP} foot refers to a downshear elongated high K_{DP} region developing left of the updraft (Romine et al. 2008). The K_{DP} foot is collocated with the downdraft region near the surface and is connected to the K_{DP} column aloft. High K_{DP} values are attributed to the presence of melting hail in observational studies (Romine et al. 2008; Bringi et al. 1986; Brandes et al. 1995; Hubbert

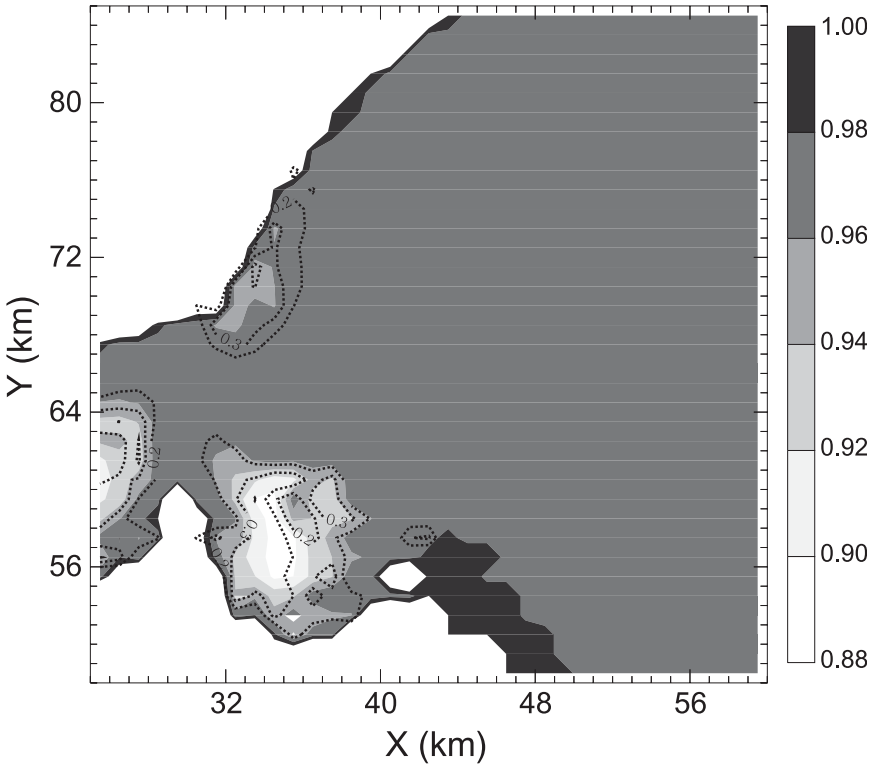

FIG. 8. As in Fig. 6d, but for simulation using the observation operator of J08. The Mie scattering effect is not included in this simple version of simulator.

et al. 1998). The supercell storm with a DM scheme exhibits all these characteristics of K_{DP} foot in Fig. 2c and Fig. 10b. The K_{DP} maximum appears in the downdraft at $z = 500$ m in Fig. 10 and is tilted upshear with height, and linked to the K_{DP} column (Fig. 2c). The K_{DP} foot structure agrees well with that of the hail mixing ratio (Fig. 6b). The SM runs produce a similar-shaped K_{DP} foot to that of the DM runs near the surface but the K_{DP} values are much too low for the SM case (Fig. 10a).

5. Summary and discussion

In this paper, a synthetic polarimetric radar simulator based on full T-matrix scattering calculations and accurate formulations for polarimetric radar variables is developed. The new simulator takes advantage of the continuous melting ice model developed in JZX08. The density of the melting ice and dielectric constant are also allowed to vary continuously. This simulator can specify any weather radar wavelength and uses up to three moments of microphysics parameterization (i.e., the total number concentrations, mixing ratios, and reflectivity factors of multiple hydrometeors) as input.

This simulator can simulate the reflectivity of the horizontal and vertical polarizations (Z_H and Z_V), differential reflectivity (Z_{DR}), specific differential phase (K_{DP}), and cross-correlation coefficient (ρ_{hv}), as well as radial velocity (V_r). These quantities are what will be observed by operational WSR-88D radars after the polarimetric upgrade and are currently being measured by the proof-of-concept polarimetric WSR-88D radar (KOUN) located in Norman, Oklahoma.

The new radar simulator is applied to an idealized supercell storm simulated using a two- or double-moment microphysics scheme. The storm with the same configurations but using a single-moment microphysics scheme is created for comparison. The simulated storm using a DM scheme exhibits unique polarimetric signatures reported in the literature, including the Z_{DR} and K_{DP} columns, Z_{DR} arc, midlevel Z_{DR} and ρ_{hv} rings, hail signature, and K_{DP} foot. Some of the signatures, mostly related to the size sorting mechanisms, however, could not be simulated when an SM scheme was used. These signatures include the Z_{DR} arc and midlevel Z_{DR} and ρ_{hv} rings. These results support that a two- or higher-moment microphysics scheme must be used to properly describe these important aspects of thunderstorms. Properly simulating these processes is also important to effectively assimilate polarimetric data into numerical models for initialization purposes.

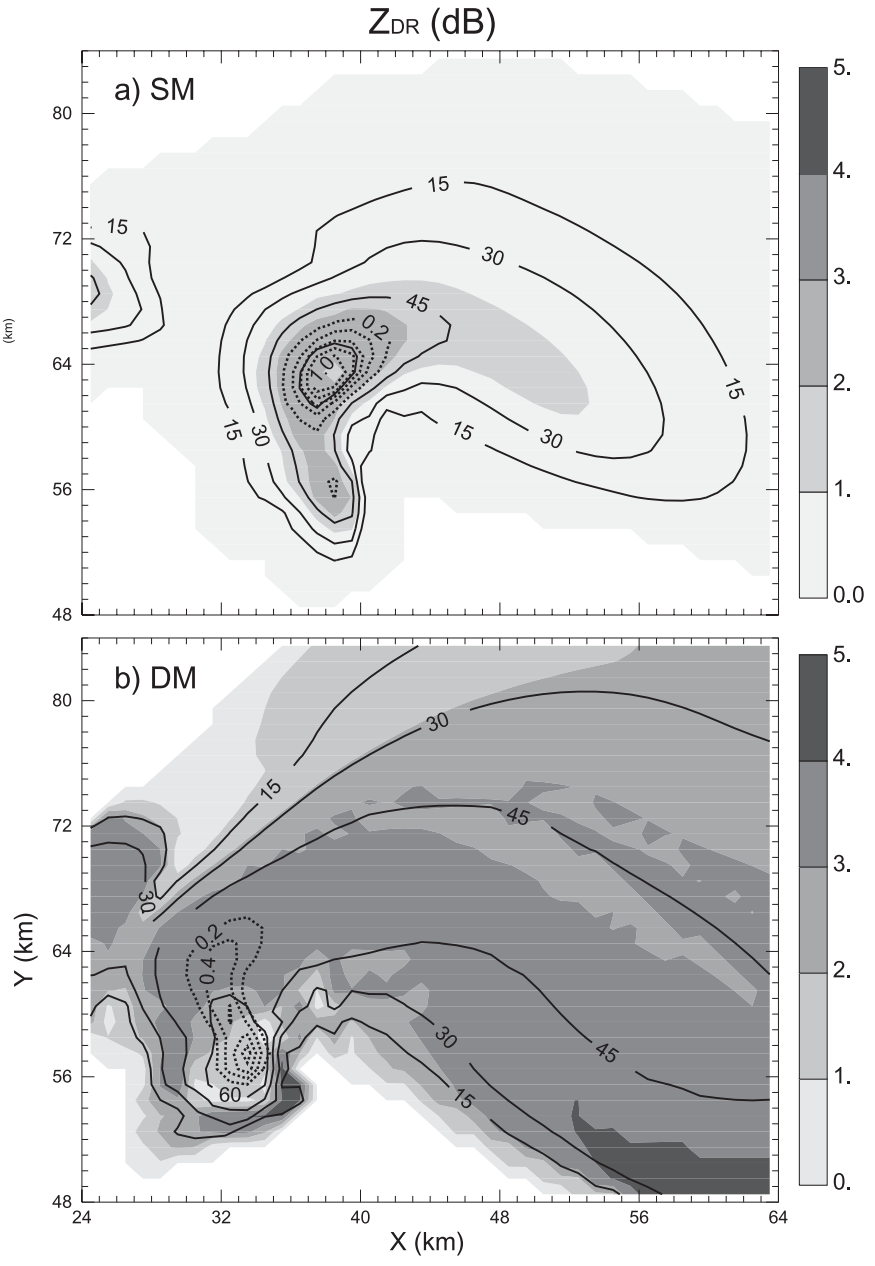

FIG. 9. The hail signature as characterized by high Z_H (thin solid contours at 15-dBZ intervals, starting at 15 dBZ) and low Z_{DR} (shading; dB) for the (a) SM and (b) DM scheme at z = 0.5 km at 70 min of simulated storm. The hail mixing ratio is overlaid in thick dotted contours at 0.2 g kg^{-1} intervals starting at 0.2 g kg^{-1}.

The verification of convective-scale numerical weather prediction is challenging because most of the model variables are not directly observed at this scale. Radar reflectivity has been used to verify the model prediction for a while. However, reflectivity alone is insufficient to verify microphysics because many independent variables and uncertain constants based on many assumptions on drop size distributions (DSDs) are involved in reflectivity calculation. Here, simulated polarimetric variables can help discriminate against and/or highlight certain variables from others by using their differential sensitivity to the water phases. They can be as useful as reflectivity because they contain additional information on the DSDs and microphysical processes. As an example, JZX08 demonstrated that a realistic radar simulator could be useful in evaluating the model microphysics

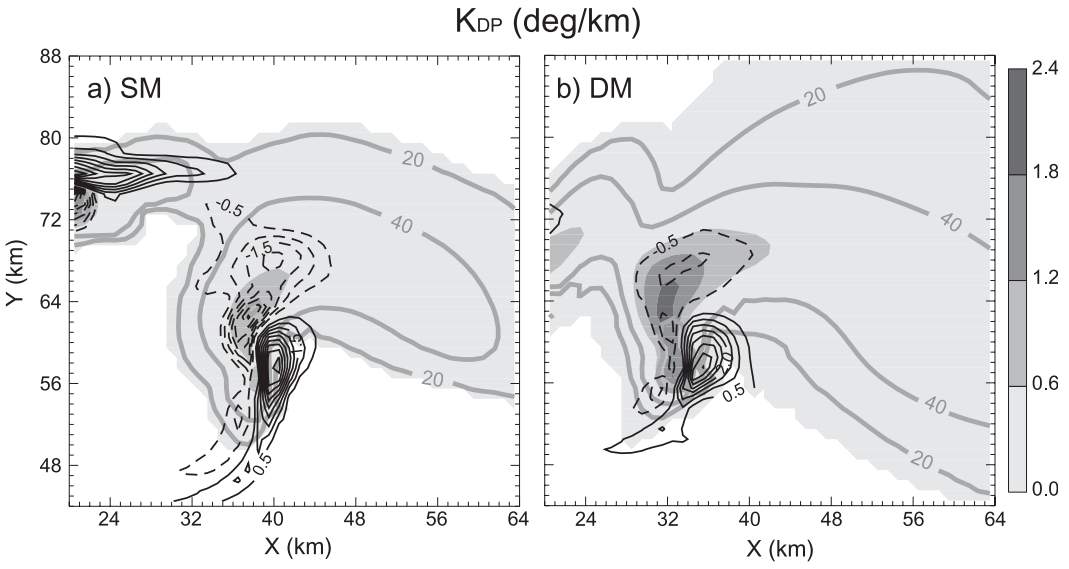

FIG. 10. The K_{DP} foot characterized by high K_{DP} (shading; $^\circ$ km^{-1}) for the (a) SM and (b) DM scheme. The vertical velocity contours are shown in dashed (downdraft; -0.5 m s^{-1} intervals) and in solid (updraft; 0.5 m s^{-1} intervals) lines, and reflectivity in solid thick gray lines (20-dBZ intervals starting at 20 dBZ) at $z = 0.5$ km at 80 min of simulated storm.

scheme by identifying delayed melting processes in the Lin-type microphysics scheme. Additionally, a realistic simulator could provide an opportunity to study storm microphysical processes in more depth.

A good radar simulator can also help forecasters determine where attention and monitoring should be directed in a high-threat situation, given convective-scale model output. KR08 related some of the polarimetric signatures to the severity of the storms: the stronger the updraft in developing storms, the stronger the Z_{DR} and K_{DP} columns; and the stronger the enhanced storm-relative environmental helicity (SREH), the stronger the Z_{DR} arc signature. This suggests that polarimetric signatures can be used as an indicator of storm intensity. Although the numerical model provides the vertical velocity as one of the prognostic variables, observed quantities can often be interpreted more intuitively. For instance, analyzing the Z_{DR} field could be as informative as examining the mixing ratio and the number concentration of each hydrometeor type separately in addition to the vertical velocity field. In this regard, the polarimetric simulator can be useful to the forecasters by providing the opportunity to look at the model polarimetric fields in advance of the occurrence of the actual event assuming the microphysical parameterization is simulating the real physical processes with a reasonable accuracy. Much research on the verification of microphysical parameterizations could help improve the reliability of synthetic polarimetric data.

Another potential for the practical use of the simulator is for it to serve as a guide to the design of future assimilation systems. The results presented in this paper suggest that assimilating Z_{DR} will likely increase the analysis error when a single-moment microphysics scheme is used in the forecast model. For example, when an SM scheme is used, the only way to simulate the Z_{DR} arc is to increase the rainwater mixing ratio at the southern edge of the forward flank when the Z_{DR} data are assimilated. However, this would increase the reflectivity in that area, which conflicts with what the observed reflectivity shows. These results suggest that it may be better not to assimilate Z_{DR} data when an SM scheme is used in the prediction model. This is an area requiring further study.

For higher frequency such as the C- and X-band radars, attenuation from the severe storm can be significant enough to alter observed polarimetric signatures, which are very different from those observed at S-band radars. In this case, an attenuation algorithm must be included to produce realistic polarimetric signatures. This will be developed as a part of the simulator in the future while a simplified version for reflectivity already exists in a data assimilation framework (Xue et al. 2009). The evaluation of both the multimoment microphysics scheme and the simulator using KOUN data is also planned for the future.

Acknowledgments. The authors thank Matthew Kumjian for useful discussion on the interpretation of

observed polarimetric signature. The authors also thank Dr. Jason Milbrandt and Daniel Dawson for helping us to use a multimoment microphysics scheme. The original T-matrix code was provided by Dr. J. Vivekanandan. This work was primarily supported by NSF Grants EEC-0313747 and ATM-0608168. Ming Xue was also supported by NSF Grants ATM-0530814, ATM-0802888, ATM-0331594, and ATM-0331756. The computations were performed at the OU Supercomputing Center for Education and Research.

REFERENCES

Beard, K. V., R. J. Kubesh, and H. T. Ochs, 1991: Laboratory measurements of small raindrop distortion. Part I: Axis ratios and fall behavior. *J. Atmos. Sci.,* **48,** 698–710.

Brandes, E. A., 1978: Mesocyclone evolution and tornadogenesis: Some observations. *Mon. Wea. Rev.,* **106,** 995–1011.

——, 1984: Vertical vorticity generation and mesocyclone sustenance in tornadic thunderstorms: The observational evidence. *Mon. Wea. Rev.,* **112,** 2253–2269.

——, 1993: Tornadic thunderstorm characteristics determined with Doppler radar. *The Tornado: Its Structure, Dynamics, Prediction and Hazards, Geophys. Monogr.,* Vol. 79, Amer. Geophys. Union, 143–159.

——, J. Vivekanandan, J. D. Tuttle, and C. J. Kessinger, 1995: A study of thunderstorm microphysics with multiparameter radar and aircraft observations. *Mon. Wea. Rev.,* **123,** 3129–3143.

——, G. Zhang, and J. Vivekanandan, 2002: Experiments in rainfall estimation with a polarimetric radar in a subtropical environment. *J. Appl. Meteor.,* **41,** 674–685.

——, ——, and ——, 2004: Comparison of polarimetric radar drop size distribution retrieval algorithms. *J. Atmos. Oceanic Technol.,* **21,** 584–598.

Bringi, V. N., R. M. Rasmussen, and J. Vivekanandan, 1986: Multiparameter radar measurements in Colorado convective storms. Part I: Graupel melting studies. *J. Atmos. Sci.,* **43,** 2545–2563.

Browning, K. A., 1964: Airflow and precipitation trajectories within severe local storms which travel to the right of the mean winds. *J. Atmos. Sci.,* **21,** 634–639.

——, and R. J. Donaldson, 1963: Airflow and structure of a tornadic storm. *J. Atmos. Sci.,* **20,** 533–545.

Capsoni, C., M. D'Amico, and R. Nebuloni, 2001: A multiparameter polarimetric radar simulator. *J. Atmos. Oceanic Technol.,* **18,** 1799–1809.

Conway, J. W., and D. S. Zrnic, 1993: A study of embryo production and hail growth using dual-Doppler and multiparameter radars. *Mon. Wea. Rev.,* **121,** 2511–2528.

Dawson, D. T., II, 2009: Impacts of single- and multi-moment microphysics on numerical simulations of supercells and tornadoes of the 3 May 1999 Oklahoma tornado outbreak. Ph.D. dissertation, School of Meteorology, University of Oklahoma, 173 pp.

——, M. Xue, J. A. Milbrandt, M. K. Yau, and G. Zhang, 2007: Impact of multi-moment microphysics and model resolution on predicted cold pool and reflectivity intensity and structures in the Oklahoma tornadic supercell storms of 3 May 1999. Preprints, *22nd Conf. on Numerical Weather Prediction,* Park City, UT, Amer. Meteor. Soc., 10B.2. [Available online at http://ams.confex.com/ams/pdfpapers/124706.pdf.]

——, ——, ——, and ——, 2010: Comparison of evaporation and cold pool development between single-moment and multimoment bulk microphysics schemes in idealized simulations of tornadic thunderstorms. *Mon. Wea. Rev.,* in press.

Doviak, R., and D. Zrnic, 1993: *Doppler Radar and Weather Observations*. 2nd ed. Academic Press, 562 pp.

Gilmore, M. S., J. M. Straka, and E. N. Rasmussen, 2004: Precipitation uncertainty due to variations in precipitation particle parameters within a simple microphysics scheme. *Mon. Wea. Rev.,* **132,** 2610–2627.

Green, A. V., 1975: An approximation for shape of large raindrops. *J. Appl. Meteor.,* **14,** 1578–1583.

Huang, G.-J., V. N. Bringi, S. van den Heever, and W. Cotton, 2005: Polarimetirc radar signatures from RAMS microphysics. Preprints, *32nd Int. Conf. on Radar Meteorology,* Albuquerque, NM, Amer. Meteor. Soc., P11R.6. [Available online at http://ams.confex.com/ams/pdfpapers/96261.pdf.]

Hubbert, J., V. N. Bringi, L. D. Carey, and S. Bolen, 1998: CSU-CHILL polarimetric radar measurements from a severe hail storm in eastern Colorado. *J. Appl. Meteor.,* **37,** 749–775.

Illingworth, A. J., J. W. F. Goddard, and S. M. Cherry, 1987: Polarization radar studies of precipitation development in convective storms. *Quart. J. Roy. Meteor. Soc.,* **113,** 469–489.

Jung, Y., 2008: State and parameter estimation using polarimetric radar data and an ensemble Kalman filter. Ph.D. dissertation, School of Meteorology, University of Oklahoma, 209 pp.

——, G. Zhang, and M. Xue, 2008a: Assimilation of simulated polarimetric radar data for a convective storm using ensemble Kalman filter. Part I: Observation operators for reflectivity and polarimetric variables. *Mon. Wea. Rev.,* **136,** 2228–2245.

——, M. Xue, G. Zhang, and J. Straka, 2008b: Assimilation of simulated polarimetric radar data for a convective storm using ensemble Kalman filter. Part II: Impact of polarimetric data on storm analysis. *Mon. Wea. Rev.,* **136,** 2246–2260.

Klemp, J. B., and R. B. Wilhelmson, 1978: Simulations of right- and left-moving thunderstorms produced through storm splitting. *J. Atmos. Sci.,* **35,** 1097–1110.

——, and M. L. Weisman, 1983: The dependence of convective precipitation patterns on vertical wind shear. Preprints, *21st Conf. on Radar Meteorology,* Edmonton, AB, Canada, Amer. Meteor. Soc., 44–49.

——, R. B. Wilhelmson, and P. S. Ray, 1981: Observed and numerically simulated structure of a mature supercell thunderstorm. *J. Atmos. Sci.,* **38,** 1558–1580.

Knight, N. C., 1986: Hailstone shape factor and its relation to radar interpretation of hail. *J. Climate Appl. Meteor.,* **25,** 1956–1958.

Kumjian, M. R., and A. V. Ryzhkov, 2008: Polarimetric signatures in supercell thunderstorms. *J. Appl. Meteor. Climatol.,* **47,** 1940–1961.

——, and ——, 2009: Storm-relative helicity revealed from polarimetric radar measurements. *J. Atmos. Sci.,* **66,** 667–685.

Lemon, L. R., and C. A. Doswell, 1979: Severe thunderstorm evolution and mesocyclone structure as related to tornadogenesis. *Mon. Wea. Rev.,* **107,** 1184–1197.

Lin, Y.-L., R. D. Farley, and H. D. Orville, 1983: Bulk parameterization of the snow field in a cloud model. *J. Climate Appl. Meteor.,* **22,** 1065–1092.

Loney, M. L., D. S. Zrnić, J. M. Straka, and A. V. Ryzhkov, 2002: Enhanced polarimetric radar signatures above the melting level in a supercell storm. *J. Appl. Meteor.,* **41,** 1179–1194.

Marshall, J. S., and W. M. Palmer, 1948: The distribution of raindrops with size. *J. Meteor.,* **5,** 165–166.

Marwitz, J. D., 1972: The structure and motion of severe hailstorms. Part I: Supercell storms. *J. Appl. Meteor.,* **11,** 166–179.

Meyers, M. P., R. L. Walko, J. R. Harrintong, and W. R. Cotton, 1997: New RAMS cloud microphysics parameterization. Part II: The two-moment scheme. *Atmos. Res.,* **45,** 3–39.

Milbrandt, J. A., and M. K. Yau, 2005a: A multi-moment bulk microphysics parameterization. Part I: Analysis of the role of the spectral shape parameter. *J. Atmos. Sci.,* **62,** 3051–3064.

——, and ——, 2005b: A multi-moment bulk microphysics parameterization. Part II: A proposed three-moment closure and scheme description. *J. Atmos. Sci.,* **62,** 3065–3081.

——, and ——, 2006: A multi-moment bulk microphysics parameterization. Part IV: Sensitivity experiments. *J. Atmos. Sci.,* **63,** 3137–3159.

Musil, D. J., A. J. Heymsfield, and P. L. Smith, 1986: Microphysical characteristics of a well-developed weak echo region in a High Plains supercell thunderstorm. *J. Climate Appl. Meteor.,* **25,** 1037–1051.

Pfeifer, M., G. C. Craig, M. Hagan, and C. Keil, 2008: A polarimetric radar forward operator for model evaluation. *J. Appl. Meteor. Climatol.,* **47,** 3202–3220.

Ray, P. S., B. Johnson, K. W. Johnson, J. S. Bradberry, J. J. Stephens, K. K. Wagner, R. B. Wilhelmson, and J. B. Klemp, 1981: The morphology of severe tornadic storms on 20 May 1977. *J. Atmos. Sci.,* **38,** 1643–1663.

Romine, G. S., D. W. Burgess, and R. B. Wilhelmson, 2008: A dual-polarization-radar-based assessment of the 8 May 2003 Oklahoma City area tornadic supercell. *Mon. Wea. Rev.,* **136,** 2849–2870.

Rosenfeld, D., and C. W. Ulbrich, 2003: Cloud microphysical properties, processes, and rainfall estimation opportunities. *Radar and Atmospheric Science: A Collection of Essays in Honor of David Atlas, Meteor. Monogr.,* No. 52, Amer. Meteor. Soc., 237–258.

Rotunno, R., 1981: On the evolution of thunderstorm rotation. *Mon. Wea. Rev.,* **109,** 171–180.

Ryzhkov, A. V., 2001: Interpretation of polarimetric radar covariance matrix for meteorological scatterers: Theoretical analysis. *J. Atmos. Oceanic Technol.,* **18,** 315–328.

——, D. S. Zrnić, and B. A. Gordon, 1998: Polarimetric method for ice water content determination. *J. Appl. Meteor.,* **37,** 125–134.

——, T. J. Schuur, D. W. Burgess, and D. S. Zrnic, 2005: Polarimetric tornado detection. *J. Appl. Meteor.,* **44,** 557–570.

Schuur, T. J., A. V. Ryzhkov, D. S. Zrnic, and M. Schonhuber, 2001: Drop size distributions measured by a 2D video disdrometer: Comparison with dual-polarization radar data. *J. Appl. Meteor.,* **40,** 1019–1034.

Tong, M., and M. Xue, 2005: Ensemble Kalman filter assimilation of Doppler radar data with a compressible nonhydrostatic model: OSS experiments. *Mon. Wea. Rev.,* **133,** 1789–1807.

Vivekanandan, J., W. M. Adams, and V. N. Bringi, 1991: Rigorous approach to polarimetric radar modeling of hydrometeor orientation distributions. *J. Appl. Meteor.,* **30,** 1053–1063.

——, V. N. Bringi, M. Hagen, and G. Zhang, 1994: Polarimetric radar studies of atmospheric ice particles. *IEEE Trans. Geosci. Remote Sens.,* **32,** 1–10.

Wakimoto, R. M., and V. N. Bringi, 1988: Dual-polarization observations of microbursts associated with intense convection: The 20 July storm during the MIST Project. *Mon. Wea. Rev.,* **116,** 1521–1539.

Waldvogel, A., 1974: The N0-jump of raindrop spectra. *J. Atmos. Sci.,* **31,** 1067–1078.

Walko, R. L., W. R. Cotton, M. P. Meyers, and J. L. Harrington, 1995: New RAMS cloud microphysics parameterization. Part I: The single-moment scheme. *Atmos. Res.,* **38,** 29–62.

Waterman, P. C., 1969: Scattering by dielectric obstacles. *Alta Freq.,* **38** (speciale), 348–352.

Weisman, M. L., and J. B. Klemp, 1982: The dependence of numerically simulated convective storms on vertical wind shear and buoyancy. *Mon. Wea. Rev.,* **110,** 504–520.

Xue, M., 2000: High-order monotonic numerical diffusion and smoothing. *Mon. Wea. Rev.,* **128,** 2853–2864.

——, K. K. Droegemeier, and V. Wong, 2000: The Advanced Regional Prediction System (ARPS) - A multiscale nonhydrostatic atmospheric simulation and prediction tool. Part I: Model dynamics and verification. *Meteor. Atmos. Phys.,* **75,** 161–193.

——, and Coauthors, 2001: The Advanced Regional Prediction System (ARPS) - A multiscale nonhydrostatic atmospheric simulation and prediction tool. Part II: Model physics and applications. *Meteor. Atmos. Phys.,* **76,** 143–165.

——, D.-H. Wang, J.-D. Gao, K. Brewster, and K. K. Droegemeier, 2003: The Advanced Regional Prediction System (ARPS), storm-scale numerical weather prediction and data assimilation. *Meteor. Atmos. Phys.,* **82,** 139–170.

——, M. Tong, and K. K. Droegemeier, 2006: An OSSE framework based on the ensemble square root Kalman filter for evaluating impact of data from radar networks on thunderstorm analysis and forecast. *J. Atmos. Oceanic Technol.,* **23,** 46–66.

——, Y. Jung, and G. Zhang, 2007: Error modeling of simulated reflectivity observations for ensemble Kalman filter data assimilation of convective storms. *Geophys. Res. Lett.,* **34,** L10802, doi:10.1029/2007GL029945.

——, M. Tong, and G. Zhang, 2009: Simultaneous state estimation and attenuation correction for thunderstorms with radar data using an ensemble Kalman filter: Tests with simulated data. *Quart. J. Roy. Meteor. Soc.,* **135,** 1409–1423.

Zhang, G., J. Vivekanandan, and E. Brandes, 2001: A method for estimating rain rate and drop size distribution from polarimetric radar measurements. *IEEE Trans. Geosci. Remote Sens.,* **39,** 830–841.